

# Large-eddy simulation study of the logarithmic law for second and higher-order moments in turbulent wall-bounded flow

Richard J.A.M. Stevens<sup>1,2</sup>, Michael Wilczek<sup>1</sup> and Charles Meneveau<sup>1</sup>

<sup>1</sup>Department of Mechanical Engineering, Johns Hopkins University, Baltimore, Maryland 21218, USA.

<sup>2</sup>Department of Science and Technology and J.M. Burgers Center for Fluid Dynamics, University of Twente, P.O Box 217, 7500 AE Enschede, The Netherlands.

(Received 7 September 2018)

The logarithmic law for the mean velocity in turbulent boundary layers has long provided a valuable and robust reference for comparison with theories, models, and large-eddy simulations (LES) of wall-bounded turbulence. More recently, analysis of high-Reynolds number experimental boundary layer data has shown that also the variance and higher-order moments of the streamwise velocity fluctuations  $u'^+$  display logarithmic laws. Such experimental observations motivate the question whether LES can accurately reproduce the variance and the higher-order moments, in particular their logarithmic dependency on distance to the wall. In this study we perform LES of very high Reynolds number wall-modeled channel flow and focus on profiles of variance and higher-order moments of the streamwise velocity fluctuations. In agreement with the experimental data, we observe an approximately logarithmic law for the variance in the LES, with a ‘Townsend-Perry’ constant of  $A_1 \approx 1.25$ . The LES also yields approximate logarithmic laws for the higher-order moments of the streamwise velocity. Good agreement is found between  $A_p$ , the generalized ‘Townsend-Perry’ constants for moments of order  $2p$ , from experiments and simulations. Both are indicative of sub-Gaussian behavior of the streamwise velocity fluctuations. The near-wall behavior of the variance, the ranges of validity of the logarithmic law and in particular possible dependencies on characteristic length scales such as the roughness scale  $z_0$ , the LES grid scale  $\Delta$ , and sub-grid scale (SGS) mixing length  $C_s\Delta$  are examined. We also present LES results on moments of spanwise and wall-normal fluctuations of velocity.

---

## 1. Introduction

The logarithmic law of the wall for the mean velocity in a rough-wall turbulent boundary layer, written below using an effective roughness scale,

$$\frac{\langle u \rangle}{u_*} = \frac{1}{\kappa} \log \left( \frac{z}{z_0} \right), \quad (1.1)$$

is a well-established result (Prandtl 1925; von Kármán 1930; Millikan 1938). Here,  $u$  is the streamwise velocity component,  $u_*$  is the friction velocity,  $\kappa \approx 0.4$  is the von Kármán constant,  $z$  is the height from the wall, and  $z_0$  is the roughness length.

Models based on the ‘attached-eddy hypothesis’ (Townsend 1976; Perry & Chong 1982; Perry *et al.* 1986) have predicted a logarithmic behavior for the variance of the fluctuations of the streamwise velocity component in the inertial layer. However, only recently

clear experimental evidence (Marusic & Kunkel 2003; Hultmark *et al.* 2012; Marusic *et al.* 2013) has emerged for a universal law for the variance (second-order moment profiles) of the streamwise velocity fluctuations, based on well-resolved experimental boundary layer data at sufficiently high Reynolds numbers. The log-law for the variance has the form

$$\langle (u'^+)^2 \rangle = B_1 - A_1 \log \left( \frac{z}{\delta} \right), \quad (1.2)$$

where  $u'^+ = (u - \langle u \rangle) / u_*$  is the normalized streamwise velocity fluctuation and  $\delta$  is an outer length scale. The experimental data are consistent with a value of  $A_1 \approx 1.25$ , i.e. the ‘Townsend-Perry’ constant (Marusic & Kunkel 2003; Smits *et al.* 2011; Hultmark *et al.* 2012; Marusic *et al.* 2013; Meneveau & Marusic 2013), while  $B_1$  depends on the flow conditions and geometry and is not thought to be universal. When Gaussian behavior is assumed, the even-order moments can be related to the second-order moment through the relationship  $\langle (u'^+)^{2p} \rangle = (2p-1)!! \langle (u'^+)^2 \rangle^p$ , where  $n!! \equiv n(n-2)(n-4) \dots 2$  is the double factorial (Meneveau & Marusic 2013). This relationship between the second and  $2p^{\text{th}}$ -moments means that the  $p^{\text{th}}$  root of the even order moments of the velocity fluctuations should follow a generalized logarithmic law for higher-order moments as follows

$$\langle (u'^+)^{2p} \rangle^{1/p} = B_p - A_p \log \left( \frac{z}{\delta} \right). \quad (1.3)$$

The assumption of Gaussian statistics furthermore implies that  $A_p = A_1 [(2p-1)!!]^{1/p}$ . The results of Meneveau & Marusic (2013) show that the experimental data are consistent with the logarithmic trends of the  $p^{\text{th}}$  root of the moments, but deviations from the Gaussian prediction for the slopes  $A_p$  are found.

Observation of such possibly canonical statistical behavior in boundary layers provides valuable points of reference for turbulence theories and various applications. Knowledge about the probability density function of velocity fluctuations plays an important role in diverse practical applications, such as characterizing wind-turbine power fluctuations to estimating probabilities of extreme events. In addition, the generalized logarithmic laws for higher-order moments may serve as a new benchmark on which to test predictions from models and simulations.

There is relatively little information available about the ability of LES to reproduce accurately higher-order statistics of turbulence. Most of the literature to date focuses on comparisons of mean velocity distributions and second-order moments. It is important to recall that most LES models are motivated by the need to dissipate kinetic energy at the correct rate, i.e. to reproduce the correct second-order statistics such as mean kinetic energy. However, there is no guarantee that the inherent nonlinear dynamics of LES will actually reproduce the extreme values of the distributions that arise from the real nonlinear dynamics in the real physical system. An earlier study (Kang *et al.* 2003) provided comparisons of LES and experiments for inertial-range velocity increments and their high-order moments in decaying isotropic turbulence. Overall, the results were encouraging. However, in wall-bounded flows the situation is significantly more challenging due to flow inhomogeneity, anisotropy, wall-blocking, etc. Prior studies on the accuracy of LES for high-Reynolds number wall-modeled turbulent boundary layers include those of Brasseur & Wei (2010), who explored various resolution criteria to reproduce accurately the mean velocity profiles, and Sullivan & Patton (2011) who documented behavior of variances and third-order moments. In this paper, we use data from high-resolution LES of a turbulent wall-bounded flow to study the ability of LES to reproduce fundamental scaling laws for second as well as higher-order moments. Such analysis has not yet been done and is needed to place LES on firmer fundamental ground as a tool to model turbulence.

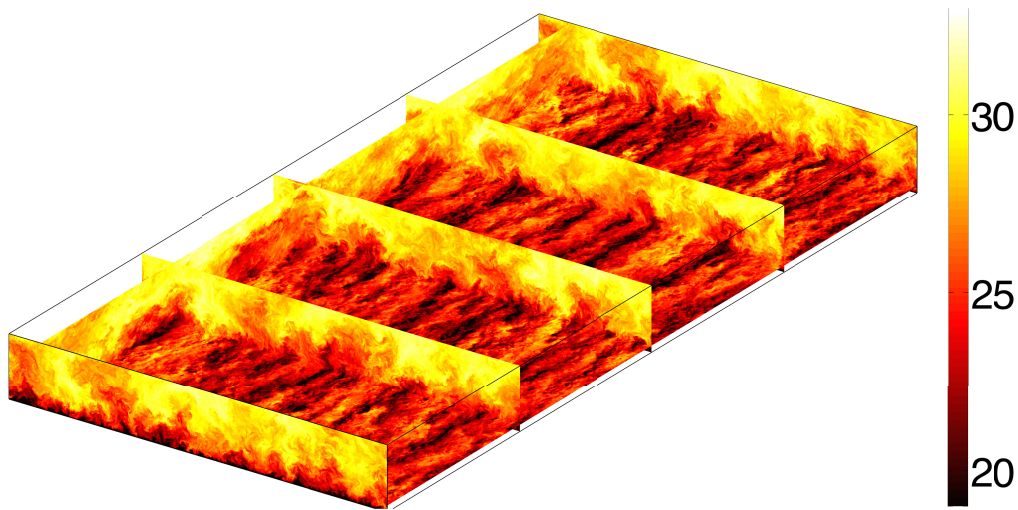


FIGURE 1. Snapshot of the streamwise velocity from the LES performed on a  $2048 \times 1024 \times 577$  grid with  $z_0/H = 1 \times 10^{-5}$  (Case I2). The color indicates the streamwise velocity in non-dimensional units  $u/u_*$ .

In section 2 we start with a brief description of the simulation method. Subsequently, in section 3.1 we compare the streamwise velocity fluctuation variance from LES with experimental data (Hutchins *et al.* 2009; Meneveau & Marusic 2013) and in section 3.2 we discuss the role of the numerical resolution and possible effects of model and physical length scales characterizing the near-wall region and in setting the lower limit of the logarithmic region for the variance. Then, in section 3.4 the spanwise and vertical velocity fluctuations are analyzed in more detail, which is followed by conclusions in section 4.

## 2. Large-eddy simulations

The LES code we use to study the turbulent wall-bounded flow solves the filtered incompressible Navier-Stokes equations without buoyancy, system rotation or other effects. The nonlinear terms are evaluated in rotational form. A pseudo-spectral discretization and thus double periodic boundary conditions are used in the horizontal directions parallel to the wall, while centered second-order finite differencing is used in the vertical direction (Moeng 1984; Albertson & Parlange 1999; Porté-Agel *et al.* 2000). The deviatoric part of the sub-grid scale stress term is modeled using an eddy-viscosity sub-grid scale model, employing the scale-dependent Lagrangian dynamic approach in conjunction with the Smagorinsky model and a sharp spectral cutoff test-filter (Bou-Zeid *et al.* 2005). Only this model will be used here, since this study is not focused on comparing the performance of different sub-grid scale models (such comparisons will be presented elsewhere). The trace of the SGS stress is combined into the modified pressure, as is common practice in LES of incompressible flow. A second-order accurate Adams-Bashforth scheme is used for the time integration. Due to the very large Reynolds numbers considered here we parameterize the bottom surface by using a classic imposed wall stress boundary condition. This boundary condition relates the wall stress to the velocity at the first grid point using the standard logarithmic similarity law (Moeng 1984) using velocities test-filtered at twice the grid scale (Bou-Zeid *et al.* 2005). This test-filtering ensures that the average predicted stress is close to the stress predicted by the classic logarithmic law. In addition the viscous stresses are neglected.

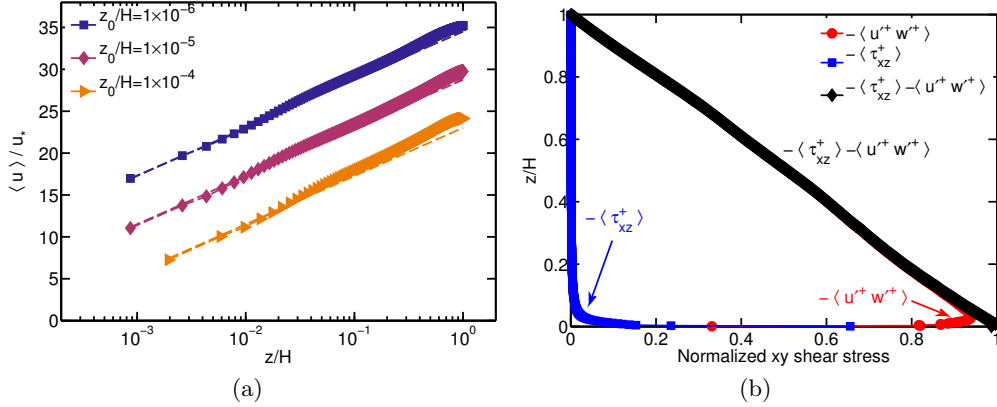


FIGURE 2. (a) Horizontally averaged streamwise velocity from LES compared with the logarithmic law for the mean flow. The squares, diamonds, and triangles indicate the results for  $z_0/H = 1 \times 10^{-6}$ ,  $z_0/H = 1 \times 10^{-5}$ , and  $z_0/H = 1 \times 10^{-4}$ , respectively, while the dashed lines are the expected corresponding log-laws. (b) Vertical profiles of the resolved stress ( $-\langle u'^+ w'^+ \rangle$ , circles) the normalized sub-grid scale stress ( $-\langle \tau_{xz}^+ \rangle$ , squares) and the total stress ( $-\langle u'^+ w'^+ \rangle - \langle \tau_{xz}^+ \rangle$ , diamonds) for  $z_0/H = 1 \times 10^{-5}$ , for case I2 (on a  $2048 \times 1024 \times 577$  grid).

The wall stress is expressed in terms of the velocity at the first grid point above the wall (at height  $\Delta z/2$  for the staggered vertical mesh,  $\Delta z$  is the vertical grid spacing) according to

$$\tau_w(x, y) = - \left[ \frac{\kappa}{\log [(\Delta z/2)/z_0]} \right]^2 \left( [\bar{u}(x, y, \Delta z/2)]^2 + [\bar{v}(x, y, \Delta z/2)]^2 \right), \quad (2.1)$$

where  $\bar{u}$  and  $\bar{v}$  indicate the test-filtered, with a spectral cutoff, streamwise and spanwise velocity. Subsequently, the stress is divided into its streamwise and spanwise component using the direction of  $\bar{\mathbf{u}}(x, y, \Delta z/2)$ . For the top boundary we use a zero-vertical-velocity and zero-shear-stress boundary condition so that the flow studied corresponds effectively to a ‘half-channel flow’ with an impermeable centerline boundary. The flow is driven by an applied pressure gradient in the  $x$ -direction, which in equilibrium determines the wall stress  $u_*^2$  and the velocity scale  $u_*$  used to normalize the results of the simulations, together with the domain height  $H$  used to normalize length scales. The LES code has been further documented and applied in various previous publications (Porté-Agel *et al.* 2000; Bou-Zeid *et al.* 2005; Chester *et al.* 2007; Calaf *et al.* 2010; Chamecki & Meneveau 2011).

As periodic boundary conditions are used in the streamwise and spanwise directions, a sufficiently large domain in these directions is required in order to allow the flow to develop with negligible correlation over the domain length. Therefore we use a domain up to  $(6\pi \times 3\pi \times 1)H$  in the streamwise, spanwise, and vertical directions, respectively. We perform simulations with different grid resolutions and roughness scale  $z_0/H$ , see table 1, to study their influence. Note that for the  $z_0/H = 10^{-6}$  case a larger domain size is used. For this case the mean velocities (compared to the friction velocity) are higher than for the higher roughnesses and, as will be explained in more detail below, we found that a larger computational domain is necessary for this case to prevent unphysical streamwise and spanwise correlations associated to the use of periodic boundary conditions. As discussed below in detail, a sufficient grid resolution is needed to accurately capture the logarithmic region for higher-order moments. In the beginning of the article we compare the simulation performed on the  $2048 \times 1024 \times 577$  grid with  $z_0/H = 10^{-5}$  (case I2) with

TABLE 1. Large-eddy simulation cases. The simulation for  $z_0/H = 10^{-4}$  and  $z_0/H = 10^{-5}$  are performed on a  $(4\pi \times 2\pi \times 1)H$  domain in the streamwise, spanwise and vertical direction, respectively, and the  $z_0/H = 10^{-6}$  cases on a  $(6\pi \times 3\pi \times 1)H$  domain. The table indicates the number of grid points used for the different cases and the ratio between the horizontal and vertical grid spacing. All simulations use the scale-dependent Lagrangian sub-grid model.

name	$z_0/H$	$N_x \times N_y \times N_z$	$\frac{\Delta x = \Delta y}{\Delta z}$	name	$z_0/H$	$N_x \times N_y \times N_z$	$\frac{\Delta x = \Delta y}{\Delta z}$
A1	$10^{-4}$	$64 \times 32 \times 32$	$2.00\pi$	E2	$10^{-5}$	$128 \times 64 \times 32$	$1.00\pi$
A2	$10^{-4}$	$128 \times 64 \times 32$	$1.00\pi$	F2	$10^{-5}$	$256 \times 128 \times 64$	$1.00\pi$
B1	$10^{-4}$	$128 \times 64 \times 64$	$2.00\pi$	G2	$10^{-5}$	$512 \times 256 \times 128$	$1.00\pi$
B2	$10^{-4}$	$256 \times 128 \times 64$	$1.00\pi$	H2	$10^{-5}$	$1024 \times 512 \times 256$	$1.00\pi$
B3	$10^{-4}$	$512 \times 256 \times 64$	$0.50\pi$	I2	$10^{-5}$	$2048 \times 1024 \times 577$	$1.13\pi$
C1	$10^{-4}$	$256 \times 128 \times 128$	$2.00\pi$	J2	$10^{-6}$	$192 \times 96 \times 32$	$1.00\pi$
C2	$10^{-4}$	$512 \times 256 \times 128$	$1.00\pi$	K2	$10^{-6}$	$384 \times 192 \times 64$	$1.00\pi$
C3	$10^{-4}$	$1024 \times 512 \times 128$	$0.50\pi$	L2	$10^{-6}$	$768 \times 384 \times 128$	$1.00\pi$
D1	$10^{-4}$	$512 \times 256 \times 256$	$2.00\pi$	M2	$10^{-6}$	$1536 \times 768 \times 256$	$1.00\pi$
D2	$10^{-4}$	$1024 \times 512 \times 256$	$1.00\pi$	N2	$10^{-6}$	$2048 \times 1024 \times 577$	$1.69\pi$

the smooth-wall experimental data collected at the University of Melbourne (hereafter the Melbourne data) at  $Re_\tau = 19,030$  (Hutchins *et al.* 2009) before we compare the LES of the cases with different roughness lengths with several experimental data sets.

In order to limit the computational time that is needed to reach a statistically stationary state, an interpolated flow field obtained from a lower resolution simulation is used as initial condition for the next, higher resolution simulation. Each case has been run for about 100 dimensionless time units (where the dimensionless time is in units of  $H/u_*$ ) before it is used as initial condition. For the simulation cases on the  $1024 \times 512 \times 256$  grid this is followed by integrating for an additional 1 dimensionless time unit on the fine grid before data collection is started. Subsequently, data are collected over roughly 2.5 time units while collecting a full snapshot of the flow field every  $\approx 0.07$  time units. For the  $2048 \times 1024 \times 577$  cases the flow is simulated for approximately 1 time unit and snapshots are saved every 0.03 time units.

A visualization of streamwise velocity normalized by  $u_*$  from a snapshot is shown in figure 1. The usual elongated structures can be seen at various distances to the wall and the increase of the variance towards the wall is also evident. In figure 2a we show that the time averaged mean velocity is close to the expected logarithmic law for the three different roughness lengths considered here, although a small ‘‘bump’’ in the log-law can be discerned at about  $z/H \approx 0.02$  to  $0.03$ , depending on the grid resolution. Many works have proposed various improvements in sub-grid and wall modeling approaches to further improve agreement with the logarithmic law for mean velocity. Here we take a well-documented model which exhibits good (but not optimized) performance in predicting the mean velocity and focus on higher-order moments of the fluctuating (resolved) velocity. The horizontally averaged vertical stress profiles in figure 2b confirm that the flow has reached a statistically stationary state in the sense that the linear shear stress profile balances the driving pressure gradient. Figure 2b shows that, due to the high resolution, the modeled normalized sub-grid scale stresses ( $-\langle \tau_{xz}^+ \rangle$ ) only become larger than 10% of the total stresses ( $-\langle \tau_{xz}^+ \rangle - \langle u'^+ w'^+ \rangle$ ) for  $z/H \lesssim 0.01$ , for the case shown

(case I2). This is also the location where the “bump” is seen in the mean velocity profile. We note that the results for the other roughness lengths are similar.

Further characterization of the LES result for case I2 is provided from the streamwise spectra shown in figure 3. The LES captures some of the expected  $k^{-5/3}$  behavior for all velocity components, although the spectra become slightly steeper for the highest wavenumbers. A peel-off at various heights can be seen that prevents a complete collapse onto a single  $-5/3$  slope due to the different values of the cutoff wavenumber when normalized with  $z$ . In the production range  $k_1 z < 1$ , for the streamwise velocity component a slope of approximately  $-1$  is observed in experiments (Perry *et al.* 1987) and in LES of atmospheric boundary layers by Porté-Agel *et al.* (2000), see figure 3a. The slope is lower for the spanwise velocity component and approximately horizontal for the vertical velocity component.

The PDFs of the velocity fluctuations in figure 3 reveal that the streamwise velocity component is sub-Gaussian, hence with a negative skewness, see figure 4a. The skewness for the three velocity components is plotted in figure 4a. The sign change of the skewness for the streamwise velocity component has also been observed in experimental data (Metzger & Klewicki 2001; Marusic *et al.* 2010) and a corresponding model has been proposed by Marusic *et al.* (2010). The spanwise and vertical velocity components are super-Gaussian, with a positive skewness for the vertical velocity component and a near zero skewness for the spanwise velocity component. For the vertical velocity component we can compare the results observed in LES of planetary boundary layers, see e.g. Sullivan & Patton (2011) and Moeng & Rotunno (1990), which is a slightly different case because the effect of the temperature inversion is not included in our simulations. Sullivan & Patton (2011) show that the change from negative to positive skewness shifts from  $z/z_i \approx 0.1$  on a  $32^3$  grid, where  $z_i$  is the inversion height, towards  $z/z_i \lesssim 0.01$  on a  $1024^3$  grid. The same trend is observed in our dataset. Apart from this near wall behavior, the LES results and measurements (Moeng & Rotunno 1990; Lenschow *et al.* 2012) are found to be consistent although we note that there is significant scatter in the measurements. The observed flatness of the vertical velocity component between 3 and 4 for  $0.05 \lesssim z/H \lesssim 0.5$  and its increase at the top of the domain are also consistent with the LES of Sullivan & Patton (2011) and recent measurements (Lenschow *et al.* 2012).

Later on we will evaluate high-order moments of the fluctuating velocities and thus statistical convergence is an important issue. As done in the analysis of experimental data (Meneveau & Marusic 2013), one can test for convergence by examining premultiplied PDFs. Figure 5 shows the premultiplied PDFs for the even-order moments up to the 10<sup>th</sup>-order. The figure shows that the moments, i.e. the area under the corresponding curves, can be determined accurately up to the 10<sup>th</sup>-order moment for the streamwise velocity component. For the spanwise and vertical velocity component we see that the statistics are slightly less converged for the 10<sup>th</sup>-order moment, but still this convergence can be considered as acceptable.

### 3. Results

In section 3.1 we compare the streamwise velocity data with experimental data from the Melbourne wind tunnel (Hutchins *et al.* 2009; Meneveau & Marusic 2013), before discussing the effect of the numerical resolution and near-wall cross-over length scales (from the near wall region to the logarithmic region for the variance) in section 3.2. Subsequently we present LES results for the spanwise and vertical velocity components in section 3.4.

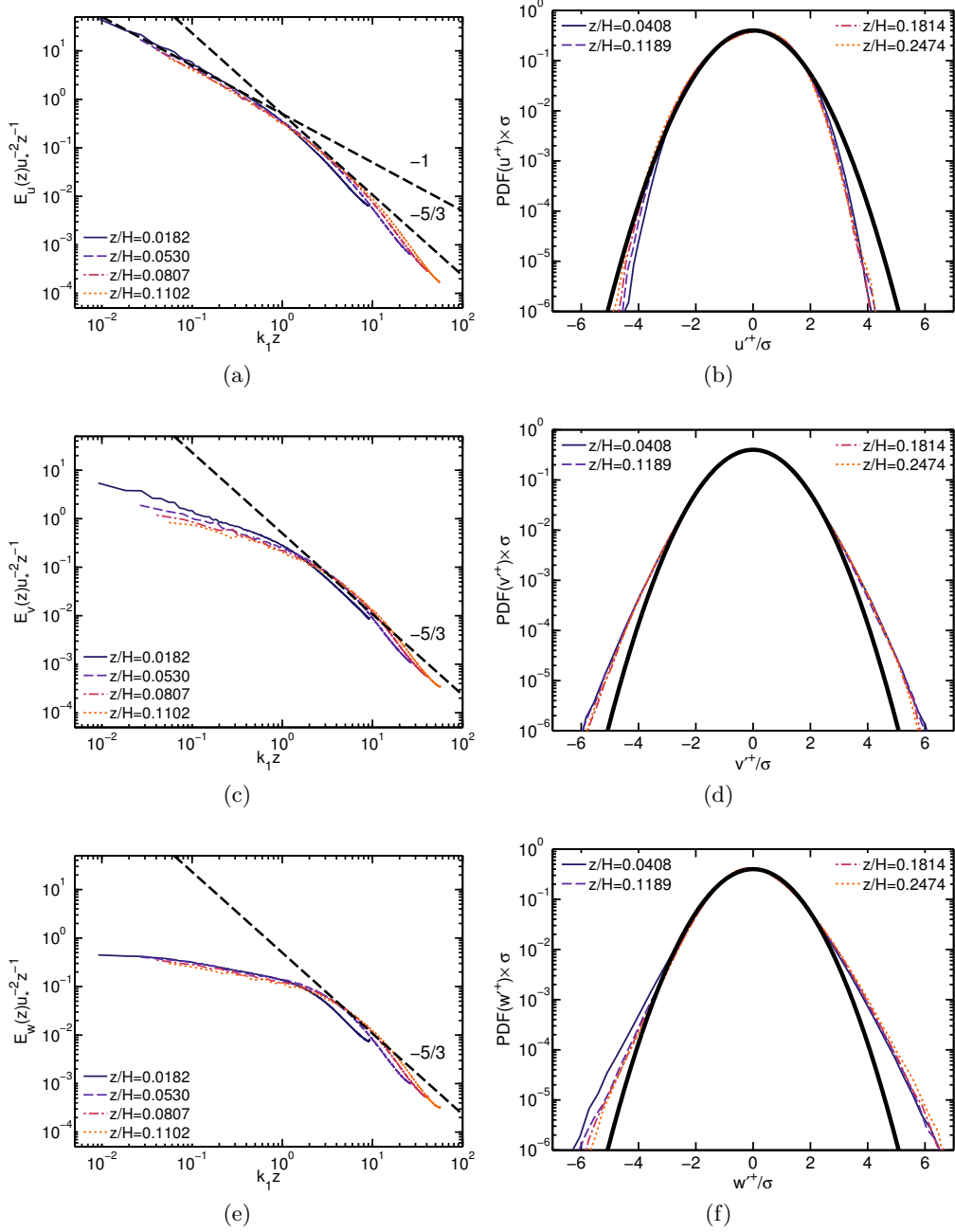


FIGURE 3. Streamwise spectra of the (a) streamwise velocity (c) spanwise velocity, and (e) vertical velocity component. Also shown are probability density functions (PDF's) for the (b) streamwise, (d) spanwise and (e) vertical velocity fluctuations at different heights. The dark line is a Gaussian distribution shown as reference.

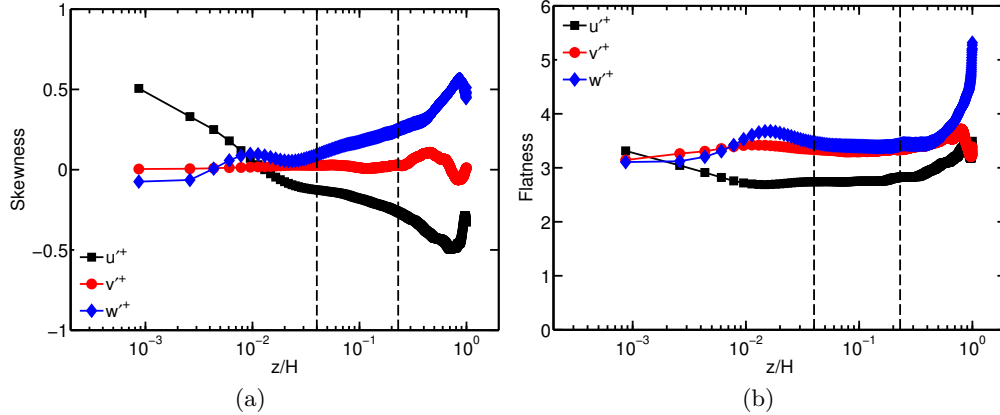


FIGURE 4. (a) Skewness and (b) flatness of the streamwise ( $u^{+}$ ), spanwise ( $v^{+}$ ) and vertical ( $w^{+}$ ) velocity component as function of  $z/H$ . The dashed vertical lines indicate the region ( $0.04 \leq z/H \leq 0.23$ ).

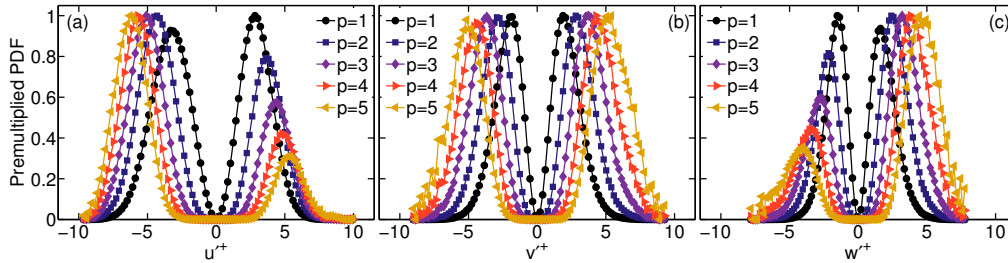


FIGURE 5. Normalized premultiplied PDFs, i.e.  $(\text{PDF}(x'^+)(x'^+)^{2p})/(\max(\text{PDF}(x'^+)(x'^+)^{2p}))$  where  $x$  indicates the (a) streamwise ( $u$ ), (b) spanwise ( $v$ ), and (c) vertical ( $w$ ) velocity component at  $z/H = 0.1189$  respectively, for  $p = 1, 2, 3, 4, 5$ . Each curve has been normalized by its peak for plotting purposes.

### 3.1. Streamwise velocity component

Figure 6a shows a comparison of the experimental (empty circles) and LES profiles of variance of streamwise velocity fluctuations. The experiments at  $Re_\tau = 19030$  from Hutchins *et al.* (2009) are plotted as function of  $z/\delta$  where  $\delta$  is the boundary layer thickness, while the LES results are plotted as function of  $z/H$ . For the data, it appears that the equivalence between the two outer scales ( $H$  for the LES and  $\delta$  for the boundary layer) appears appropriate, since no additional horizontal shifting is seen to be required. The agreement between the LES and the data is quite good for  $z/H \gtrsim 0.02$ , with a logarithmic layer for the variance visible from about  $z/H \approx 0.23$  down to about  $z/H \approx 0.02$ . This is further confirmed by examining the local slope plot in Fig. 6b, which displays good agreement between LES and experiment down to  $z/H \approx 0.02$ . The vertical dashed lines indicate the suggested range of the logarithmic region for the variance, and within this region the slope is  $A_1 \approx 1.25$  shown as the dashed line in Fig. 6a.

Note that the reported profiles for the variance from LES corresponds to the ‘resolved’ part of the fluctuations and do not include the sub-grid scale variance. In order to verify that the sub-grid scale variance can be neglected in the logarithmic region for the variance  $0.04 \leq z/H \leq 0.23$ , we examine the variance spectra, see figure 3, in more detail. The



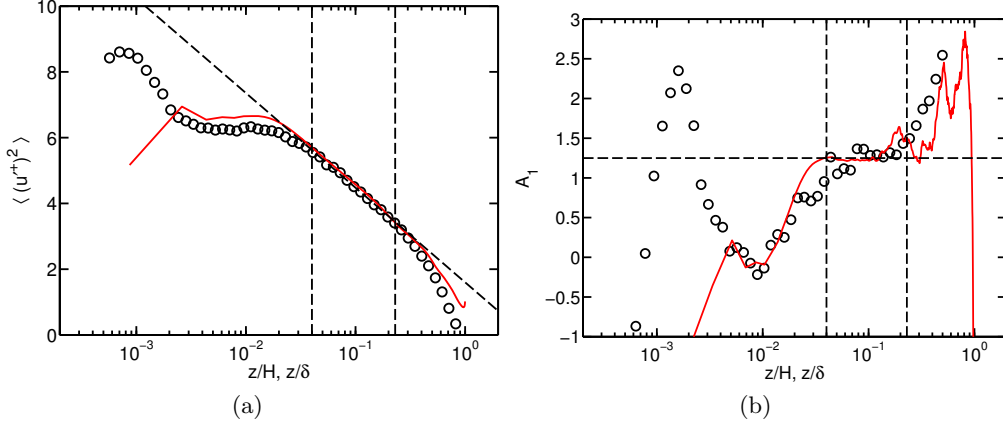


FIGURE 6. (a) Profile of second-order moment for the streamwise velocity fluctuations obtained from LES (line) compared with the experimental results (circles) (Hutchins *et al.* 2009; Meneveau & Marusic 2013) as function of  $z/H$  ( $z/\delta$ ). The dashed line is the fitted logarithmic law for the variance. (b) The local  $A_1$  (local slope), see (1.3), as function of  $z/H$ . The dashed vertical lines indicate the region ( $0.04 \leq z/H(z/\delta) \leq 0.23$ ) over which  $A_1$  is determined. LES grid locations are shown in figure 2 to 4, figure 7 and figure 16.

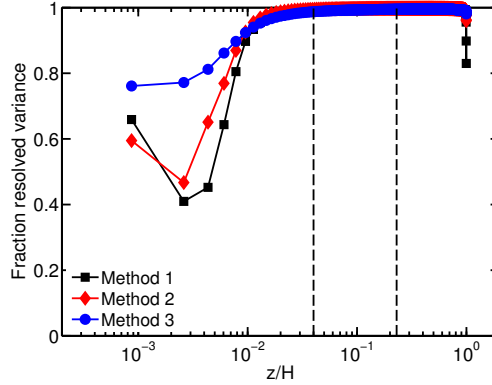


FIGURE 7. The fraction of the resolved variance of  $u$ ,  $\sigma_{u\text{-LES}}^2/\sigma_{u\text{-total}}^2$  as function of  $z/H$  determined by extrapolation the spectra towards infinity obtained using three different methods, see details in text. The dashed vertical lines indicate the region ( $0.04 \leq z/H \leq 0.23$ ). Closer towards the wall where the fraction of the resolved variance is lower the determination becomes less accurate.

second-order moment is related to variance spectra as follows

$$\langle (u'^+)^2 \rangle = \sigma_{u\text{-LES}}^2 = 2 \int_0^{k_{\max}} E_u(k_1; z) u_*^{-2} dk_1, \quad (3.1)$$

where  $E_u(k_1; z)$  is the 1-D variance spectrum of the streamwise velocity component in the streamwise wavenumber direction, at height  $z$ . The integration is over the resolved wavenumber range, from 0 to  $k_{\max}$ , where  $k_{\max}$  is the largest resolved wavenumber in the LES. By extrapolating the spectra toward infinity the resolved variance in the streamwise velocity component can be compared to its assumed true value. We provide estimates for the total variance by extrapolating the spectrum towards  $\infty$  (for practical purposes we

approximate infinity with  $10000k_{\max}$ ) and using

$$\sigma_{\text{u-total}}^2 = \sigma_{\text{u-LES}}^2 + 2 \int_{k_{\max}}^{\infty} E_{\text{model}}(k_1; z) u_*^{-2} dk_1, \quad (3.2)$$

where the second term (the SGS variance, which we will also denote as  $\sigma_{\text{u-SGS}}^2$ ) is calculated from an extrapolated spectrum from the LES data. We use three ways to specify  $E_{\text{model}}$  used in the second term. The first method is a least squares fit to the LES spectrum from  $k_{\max}/2$  until  $k_{\max}$ , the second method a least squares fit to the LES spectrum from  $k_{\max}/2$  until  $3k_{\max}/4$  and the third method using a  $-5/3$  spectrum starting at  $k_{\max}$ . The result of this procedure is shown in figure 7 and shows that for  $0.02 \leq z/H \leq 0.95$  more than 98% of the variance in the flow is resolved by our LES, and for most heights it is more than 99%. We note that these observations are qualitatively consistent with the observation that the modeled normalized sub-grid scale stresses ( $-\langle \tau_{xz}^+ \rangle$ ) only become larger than 10% of the total stresses ( $-\langle \tau_{xz}^+ \rangle - \langle u'^+ w'^+ \rangle$ ) for  $z/H \lesssim 0.01$ , see figure 1b. Here we emphasize that different methods could be used to estimate the sub-grid scale variance, which could lead to slightly different results. Therefore the mentioned fraction of the resolved variance and the corresponding sub-grid scale variance should be considered as an approximation only. As is shown in figure 7 the uncertainty becomes larger closer to the wall due to the difficulties in estimating the sub-grid scale variance when the resolved variance in the flow is only in the order of 50% which happens in the first few grid-points above the wall. Here we also emphasize that the mean and variance profiles obtained from LES are relatively resolution independent in the well resolved region of the flow, while differences are observed closer to the wall where the resolution influences the resolved variance in the flow most.

Next, in figure 8a we present profiles of moments of order  $2p$ , raised to the power  $1/p$ . It shows that the higher-order, even moments of the streamwise velocity also agree quite well with the experimental data. In agreement with this observation the corresponding  $A_p$  values (see (1.3)) obtained from fitting the data in the interval  $0.04 \leq z/H \leq 0.23$  also show good agreement, see figure 8b.

### 3.2. Cross-over scale

Estimates for the near-wall start of the logarithmic region for the variance vary significantly. The classical theoretical assumption is that the equilibrium logarithmic layer begins at a fixed value of  $z^+$ . However, recent experimental evidence (Zagarola & Smits 1998; Marusic & Kunkel 2003; Hutchins *et al.* 2009; Winkel *et al.* 2012; Hultmark *et al.* 2012; Hutchins *et al.* 2012; Marusic *et al.* 2013) and studies such as those of Wei *et al.* (2005), Eyink (2008), and Klewicki *et al.* (2009) suggest that there is a Reynolds-number dependence for the lower limit of this region. Specifically, Klewicki *et al.* (2009), Alfredsson *et al.* (2011) and Marusic *et al.* (2013) have proposed a  $\sim Re_\tau^{1/2}$  dependence for the lower limit of the logarithmic law for the variance. At very high Reynolds numbers, such a trend raises the interesting question about how to represent effects of viscosity in ‘infinite Reynolds number’ LES in which the viscous stress is neglected entirely. Also, the status of such a scaling for rough-wall boundary layers has not been established. Here we examine this issue from the viewpoint of our LES results. In general agreement with observations from experimental data (Marusic & Kunkel 2003; Hutchins *et al.* 2009; Smits *et al.* 2011; Kulandaivelu 2012; Winkel *et al.* 2012; Hultmark *et al.* 2012; Hutchins *et al.* 2012; Marusic *et al.* 2013) we find that the turbulence intensity profiles tend to depart more abruptly from the logarithmic profile for the variance than profiles of the mean velocity when approaching the wall. Figure 6 shows the LES data begin to deviate from the logarithmic law for the variance when  $z/H \lesssim 0.02$ . We point out that also at

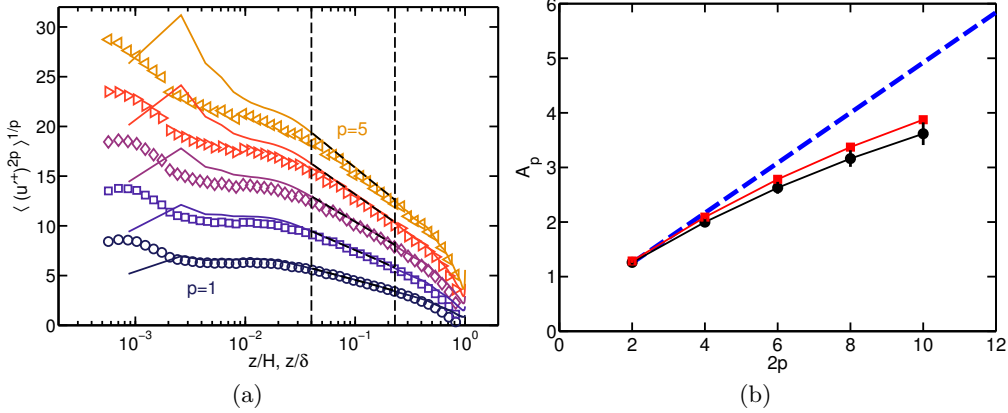


FIGURE 8. (a) Even-order moments (raised to the  $1/p$ -th power), of order  $2p = 2$  (circles), 4 (squares), 6 (diamonds), 8 (right-pointing triangles), and 10 (left-pointing triangles) of the streamwise velocity fluctuations as a function of  $z/H$  ( $z/\delta$ ). The symbols indicate experimental data (Hutchins *et al.* 2009; Meneveau & Marusic 2013) and the lines LES data. The dashed vertical lines indicate the logarithmic region for the variance ( $0.04 \leq z/H(z/\delta) \leq 0.23$ ). (b)  $A_p$  as function of  $2p$  from the Melbourne experiments at  $Re_\tau = 19,030$  (circles) and LES (squares). The dashed line indicates the Gaussian values  $A_p = A_1[(2p-1)!!]^{1/p}$  with  $A_1 = 1.25$ . LES grid locations are shown in figure 2 to 4, figure 7 and figure 16.

this height the mean velocity displays a non-negligible ‘‘bump’’ as seen in figure 2 around the twelfth vertical grid point, i.e.  $z/H \approx 0.02$ .

In the LES, since viscous effects are neglected, there are only a few other characteristic length scales in the near-wall region: the grid resolution  $\Delta$  (here we use the simplifying characterization of grid scale as  $\Delta = (\Delta x \Delta y \Delta z)^{1/3}$ , see Scotti *et al.* (1993) for a justification), the LES mixing length  $C_s \Delta$ , where  $C_s$  is the dynamically determined Smagorinsky coefficient, and the imposed roughness scale  $z_0$ . We will denote the height of the break in the variance profiles as  $z_b$ . One can postulate a simple extension of the two prior models for the lower limit of the logarithmic layer for the variance (fixed  $z_b^+$ , or additional dependence on Reynolds number as  $z_b^+ Re_\delta^{1/2}$ ) to the case of LES in which an ‘LES inner length-scale’ replaces the viscous scale,  $\nu/u^*$ . Then one is led to four possibilities: that the cross-over scales with grid resolution and then it could occur at either a fixed height  $z_b/\Delta$ , or at a fixed  $\Delta(z_b/\Delta)^{1/2}$  (or with the corresponding mixing length  $C_s \Delta$  instead of  $\Delta$ ). Or that the cross-over scales with roughness length  $z_0$ , again leading to two possibilities: a cross-over at a fixed height  $z_b/z_0$  or at a fixed  $z_0(z_b/z_0)^{1/2}$ . Naturally, some other powers may be possible, or if  $\Delta/H$  is close to  $z_0/H$  some intermediate options are possible, including dependencies on both  $\Delta/H$  and  $z_0/H$ .

We first examine the dependence of the cross-over on grid resolution  $\Delta$ . As discussed before, the spectra (figure 3) and the vertical stress profiles (figure 2b) indicate that a smaller fraction of the variance of the flow is explicitly resolved in this region and the LES modeling therefore becomes more important. The reason for this is that here the horizontal resolution becomes more limiting and at the same time the effect of the modeled wall stresses (see (2.1)) becomes noticeable in this region. The results indicate that the position at which the LES data for the higher-order moments begin to depart from the logarithmic law depends on the grid resolution. As there is uncertainty in the determination of  $z_b$ , especially for lower resolution simulations, we find this location using two methods. In the first method we define  $z_b/H$  based on the vertical location where

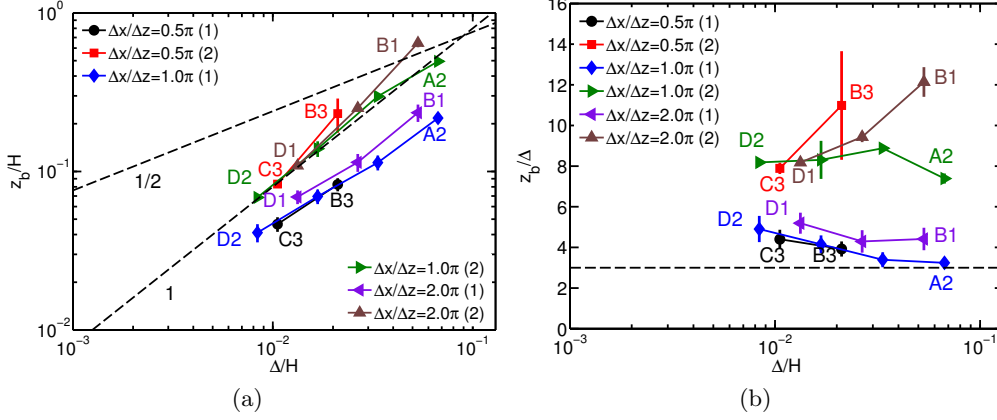


FIGURE 9. (a)  $z_b/H$  as function of  $\Delta/H$  compared to  $(\Delta/H)^1$  and  $(\Delta/H)^{1/2}$  behavior (dashed lines). (b)  $z_b/\Delta$  as function of  $\Delta/H$ . The circles, diamonds, and left-pointing triangles indicate  $z_b/H$  obtained from  $A_1 = 1$  ((1) in the legend). The squares, right-pointing triangles, and up-pointing triangles indicate  $z_b/H$  obtained from  $dA_1/dz = 0$  ((2) in the legend), see details in the text. The ratio of the horizontal to vertical grid scale is mentioned in the legend, see also table 1.

$A_1 = 0.8$ , see figure 2b. In the second method  $z_b/H$  is based on the position where  $dA_1/dz=0$ . Figure 9 shows  $z_b/H$  as function of  $\Delta/H$  assuming  $z_b > 3\Delta$ . The  $z_b > 3\Delta$  criterion is used to prevent that the first local maximum in the  $A_1$  as function of  $z/H$  profiles, see figure 6b, is identified as the start of the logarithmic region for the variance. For the first method the uncertainty is based on the difference between  $z_b$  obtained using  $A_1 = 0.6$  and  $A_1 = 1.0$ . For the second method the uncertainty gives the difference in  $z_b/H$  obtained using  $A_1$  and  $A_1$  smoothed over a  $3\Delta z$  interval. The figure shows that the lower boundary at which the logarithmic region for the variance can be observed shifts towards the wall when the grid spacing is decreased. Because the outer boundary of the logarithmic region for the variance occurs at a fixed fraction of the boundary layer thickness (about  $0.1\delta$  to  $0.2\delta$ ), this means that a sufficient resolution is required to capture the logarithmic region for the variance over a significant interval. For our highest resolution simulation the start of the logarithmic region for the variance is identified to be around  $z/H \approx 0.02$  and for some of the lower resolution simulation the logarithmic region for the variance that can be resolved is too small to observe it clearly. Although the data in figure 9 show that a small power difference with  $(\Delta/H)^1$  dependence cannot be excluded, certainly a scaling with  $(\Delta/H)^{1/2}$  does not appear to hold.

Figure 10 shows that for all simulations, except for the two lowest resolution simulation (A1 and A2 (see table 1); case A1 is omitted from these graphs as  $z_b$  cannot be determined well for that simulation) the sub-grid scale variance is less than 10% at  $z_b$  and this decreases strongly with increasing resolution. Figure 10b reveals, in agreement with figure 9a, that the results reasonably collapse when represented as function of  $z_b/\Delta$ . Figure 11 shows  $z_b/H$  as function of  $C_s\Delta/H$  and  $z_b/(C_s\Delta)$  as function of  $C_s\Delta/H$ . As the  $C_s$  value at  $z_b/H$  is relatively constant, the message of the corresponding figure is similar to the one shown in figure 9, and considering the uncertainty in the data it is hard to say whether  $C_s\Delta$  or  $\Delta$  length scale is most appropriate.

Next, we examine the possible dependence of the cross-over height  $z_b/H$  on the imposed roughness scale  $z_0/H$ . Figure 12 shows the second-order moments of fluctuating streamwise velocity for the simulations and several experiments with the different  $z_0/H^*$

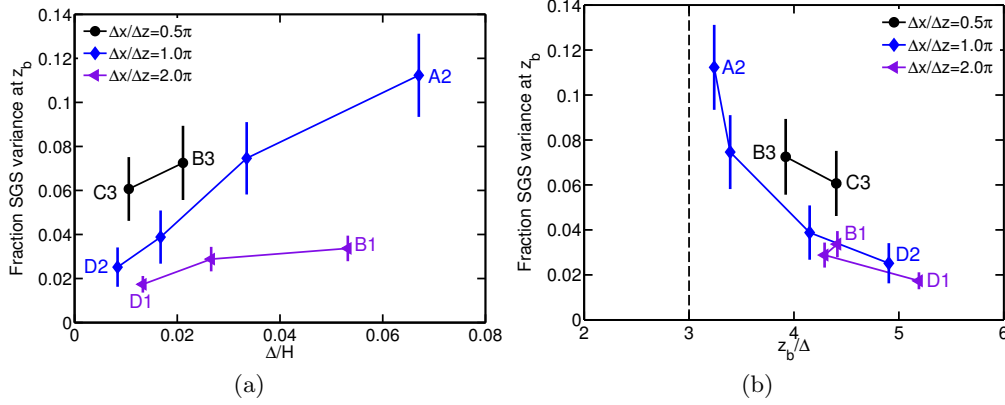


FIGURE 10. The fraction of SGS variance,  $\sigma_{u-\text{LES}}^2/\sigma_{u-\text{total}}^2$ , at the lowest  $z_b/H$ , see figure 9, as function of (a)  $\Delta/H$  and as function of (b)  $z_b/\Delta$  using the lower  $z_b$  estimates shown in figure 9. Panel a shows that the percentage of the SGS variance decreases with increasing grid resolution (decreasing  $\Delta$ ). Panel b shows that the results nearly collapse with the  $z_b/\Delta$  relation found. Note that the  $z_b > 3\Delta$  criterion is such that the determined  $z_b$  value is not directly influenced for the shown results. The vertical bars indicate the variation obtained from the different methods to determine the SGS variance.

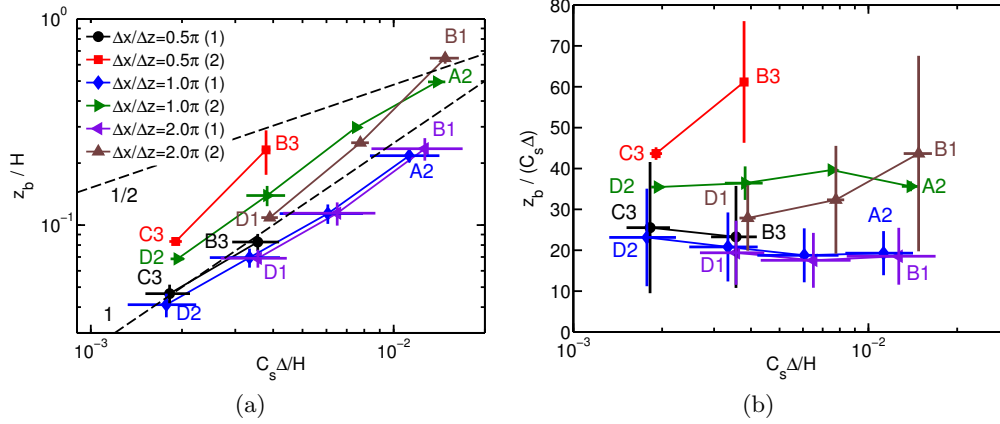


FIGURE 11. (a)  $z_b/H$  as function of  $C_s\Delta/H$  compared to  $(C_s\Delta/H)^1$  and  $(C_s\Delta/H)^{1/2}$  behavior (dashed lines). (b)  $z_b/(C_s\Delta)$  as function of  $C_s\Delta/H$ . The circles, diamonds, and left-pointing triangles indicate  $z_b/H$  obtained from  $A_1 = 1$  ((1) in the legend). The squares, right-pointing triangles, and up-pointing triangles indicate  $z_b/H$  obtained from  $dA_1/dz = 0$  ((2) in the legend), see details in the text. The ratio of the horizontal to vertical grid scale, as well as the simulation case numbers as defined in table 1 are indicated. The horizontal and vertical bars indicate the uncertainty determined as indicated in the text.

and  $z_0/\delta^*$ , and the corresponding local  $A_1$ . Here  $H^*$  and  $\delta^*$  are chosen such that all the shown data sets overlap in order to focus on  $A_1$  and not on  $B_1$ , which is discussed below. From figure 13 we conclude that  $z_b/H$  is roughly independent of  $z_0/H$ . Simulations using larger roughness lengths (i.e.  $z_0/H = 2 \times 10^{-4}$ , not shown) and at high resolution suggest that when  $z_0/H$  is no longer much smaller than  $\Delta/H$ , the assumptions on which the equilibrium wall boundary condition is based, begin to lose validity and results (not shown) are degraded. In figure 12a one can also notice that the fluctuations close to the

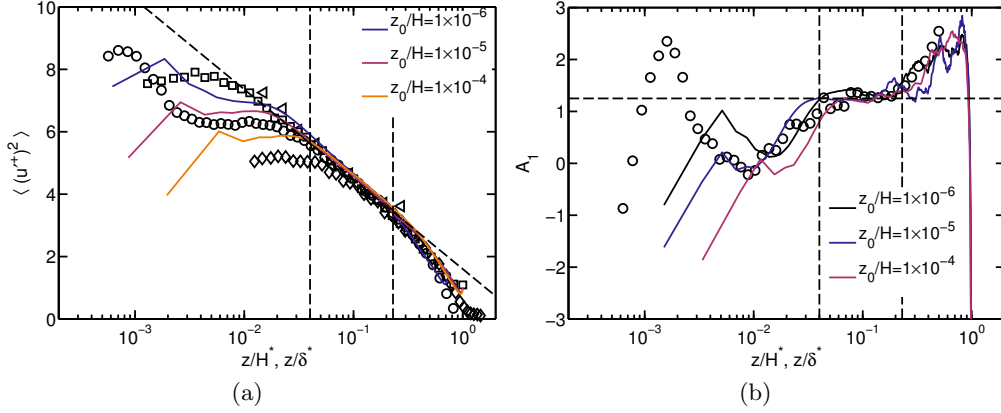


FIGURE 12. (a) Profile of second-order moment for the streamwise velocity fluctuations obtained from LES compared with the experimental results as function of  $z/H^*$  ( $z/\delta^*$ ). (b) The local  $A_1$ , see (1.3). The colors indicate the different  $z_0/H^*$  values from the LES. The symbols indicate different experimental data sets: diamonds (roughness, Schultz & Flack (2007)), circles (Melbourne, Hutchins *et al.* (2009)), squares (Superpipe, Hultmark *et al.* (2012)), triangles (SLTEST, Hutchins *et al.* (2012)). LES grid locations are shown in figure 2 to 4, figure 7 and figure 16.

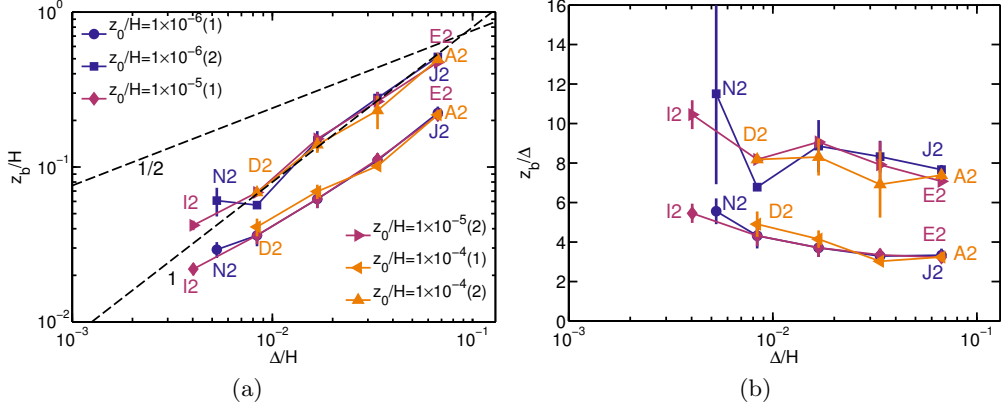


FIGURE 13. (a)  $z_b/H$  as function of  $\Delta/H$  compared to  $(\Delta/H)^1$  and  $(\Delta/H)^{1/2}$  behavior (dashed lines) plotted for various  $z_0$  to quantify dependence on  $z_0$ . (b)  $z_b/\Delta$  as function of  $\Delta/H$ . The circles, diamonds, and left-pointing triangles indicate  $z_b/H$  obtained from  $A_1 = 0.9$  ((1) in the legend). The squares, right-pointing triangles, and up-pointing triangles indicate  $z_b/H$  obtained from  $dA_1/dz = 0$  ((2) in the legend), see details in the text. The  $z_0/H$  value is indicated in the legend, see also table 1.

wall decrease with increasing roughness. The reason is that the rougher surface will result in a larger damping of the streamwise velocity fluctuations close to the wall. In figure 12b we see that this results in a slight decrease of  $A_1$  as function of the roughness length. We note that the differences in the local  $A_1$  obtained for the different roughness lengths in the LES are mainly due to the difference in the resolutions used for these cases.

Figure 14a shows  $A_1$  obtained from the region  $0.04 \leq z/H \leq 0.23$  compared to the experimental data from several high  $Re$  number experiments as summarized in table 1 of Marusic *et al.* (2013). In order to relate the inner scale between our LES and the

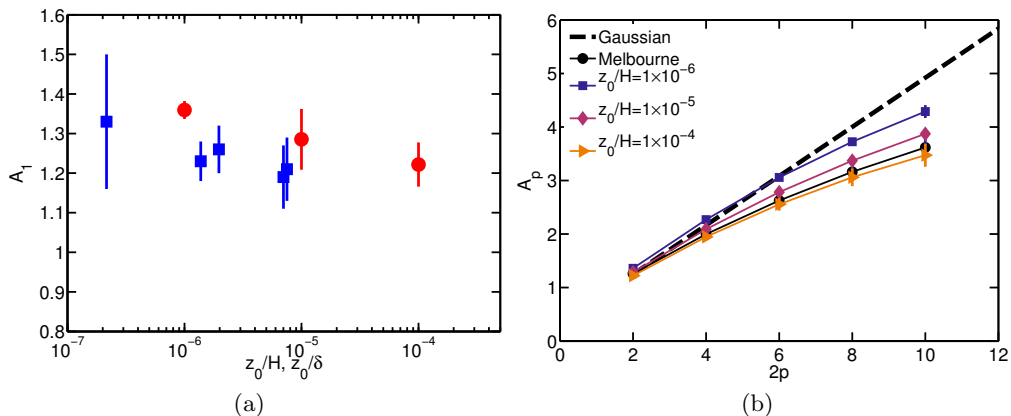


FIGURE 14. (a)  $A_1$  as function of  $z_0/H$  ( $z_0/\delta$ ) for different experiments (squares, Marusic *et al.* (2013)) and the LES (circles). Note that for the experimental data  $z_0/\delta$  is obtained from (3.3) as described in the text. (b)  $A_p$  as function of  $2p$  from experiments (circles) and LES with the different  $z_0/H$ . The dashed line indicates the Gaussian comparison  $A_p = A_1[(2p-1)!!]^{1/p}$  with  $A_1 = 1.25$ .

experimental data on smooth wall boundary layers we use the approximate relationship

$$\frac{z_0}{\delta} = \frac{\nu}{\delta u_*} \exp(-\kappa B), \quad (3.3)$$

where  $\nu$ ,  $u_*$  and  $\delta$  are the air viscosity, friction velocity and boundary layer height in the experiment. The empirical values  $\kappa = 0.4$  and  $B = 5$  and the  $\nu$ ,  $u_*$  and  $\delta$  values as documented in table 1 of Marusic *et al.* (2013) are used.

As the  $B_1$  value in the logarithmic law for the variance depends on the large-scale flow geometry (e.g. it is expected to differ for channels and boundary layers), and because we are mainly interested in capturing the “universal” slope  $A_1 = 1.25$  behavior, we show the data in figure 12a as function of  $z/H^*$ . For the experiments the uncertainties shown as error bars are the ones given in table 1 and 2 of Marusic *et al.* (2013). For the LES we determine the uncertainty in the same way as done for the experimental data (Marusic *et al.* (2013)) by determining the 95% confidence bounds from the curve-fitting procedure. In order to obtain values consistent with the experimental ones we interpolate the LES data to the measurements heights used in the experiments. The figure suggests that  $A_1$  slowly decreases with increasing roughness although the trend is weak compared to the uncertainties. We also recall the observation of Meneveau & Marusic (2013) that  $A_p$  for the higher-order moments becomes less sensitive to  $Re_\tau$  for increasing Reynolds number. Additional experimental and simulation results are needed to verify whether an actual  $z_0$  dependence exists.

### 3.3. The role of $B_1$

In contrast to the fairly constant  $A_1$  value it has been shown by Marusic *et al.* (2013) that  $B_1$  can vary significantly among different flows, indicative of dependencies on non-universal large-scale structures in turbulent wall-bounded flows. The data in figure 14 show the observed variation of  $B_1$  as function of  $z_0/H$ . The figure shows that  $B_1$  obtained from LES is within the scatter obtained from the experiments. Since the half-channel flow geometry in our LES differs from the developing boundary layer experiments, to the degree that there are differences, these are to be expected. One can notice that the  $B_1$  value obtained from LES is higher for  $z_0/H = 10^{-6}$  than for the other two LES

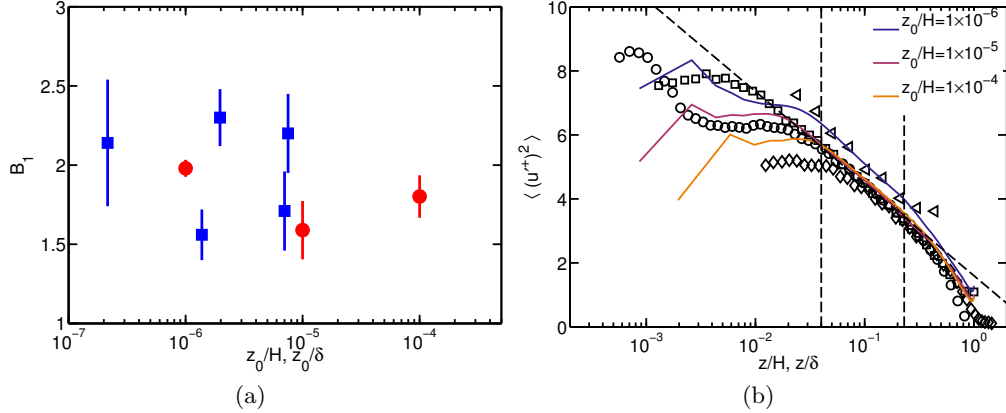


FIGURE 15. (a)  $B_1$  as function of  $z_0/H$  ( $z_0/\delta$ ) for different experiments (squares, Marusic *et al.* (2013)) and the LES (circles). Note that for the experimental data,  $z_0/\delta$  is obtained from (3.3) as described in the text. (b) Symbols indicate different experimental data sets: diamonds (rough wall boundary layer, Schultz & Flack (2007)), circles (Melbourne, Hutchins *et al.* (2009)), squares (Superpipe, Hultmark *et al.* (2012)), triangles (SLTEST, Hutchins *et al.* (2012)). LES grid locations are shown in figure 2 to 4, figure 7 and figure 16.

cases. We are not sure what the reason is for this difference. The  $z_0/H = 10^{-6}$  case is the more challenging case since its lower roughness leads to higher mean velocities (compared to the friction velocity). As the increase in the velocity fluctuations is small compared to the increase in the mean velocity, the turbulence intensity is significantly lower for this case than for the other cases. Therefore a larger computational domain to prevent unphysical streamwise and spanwise correlations associated to the use of periodic boundary conditions is necessary. A too small domain leads to higher fluctuations. In addition, the  $\Delta/z_0$  and  $(\Delta_x = \Delta_y)/\Delta_z$  are largest for  $z_0/H = 10^{-6}$ , which could influence the results. However, unfortunately it is at the moment not possible to perform the  $z_0/H = 10^{-6}$  with the same  $\Delta/z_0$  and  $(\Delta_x = \Delta_y)/\Delta_z$  as the other cases since this would require grids with more than an order of magnitude more grid points.

#### 3.4. Spanwise and normal velocity components

We now turn to the fluctuations of the spanwise velocity component. Figure 15a shows the higher-order moment data obtained from LES for the spanwise fluctuations. The data in this figure do not reveal as clear a logarithmic region for the variance as the streamwise component results. As indicated before, the spanwise velocity fluctuations are more difficult to resolve than the streamwise velocity fluctuations since their characteristic length scales tend to be smaller than the elongated ones in the streamwise direction. This probably means that the results for the spanwise velocity component are more sensitive to the numerical resolution than for the streamwise velocity component. As we have seen in the previous section that the logarithmic region for the variance of the streamwise velocity can only be captured clearly when the grid is sufficiently fine, we cannot exclude that LES at significantly higher spanwise resolution could reveal a logarithmic region for the spanwise velocity fluctuations as well, but we believe this observation cannot be made based on the current dataset.

In contrast to the streamwise and spanwise velocity fluctuations, the higher-order moments for the vertical velocity fluctuations shown in figure 15b do not reveal any logarithmic region for the variance. Because the vertical velocity fluctuations seem to decrease linearly starting from the outer boundary of the logarithmic region up to ap-



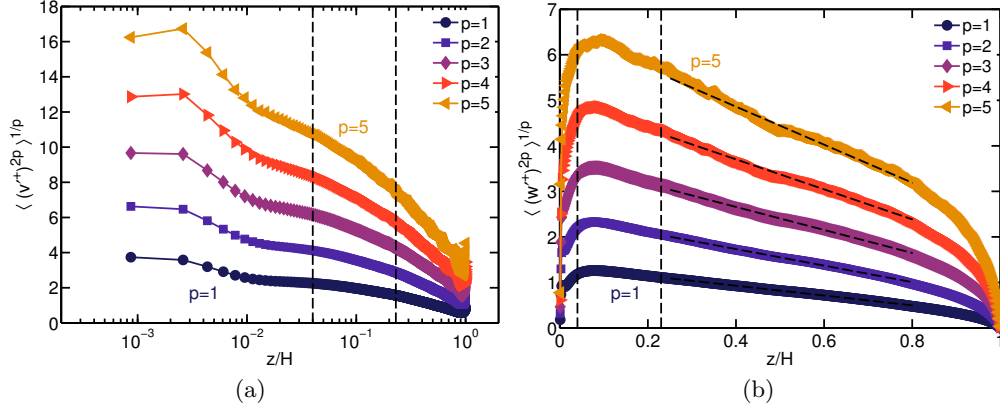


FIGURE 16. From bottom to top the figure indicates the moments of order  $2p = 2, 4, 6, 8,$  and  $10$  as a function of  $z/H$  for the (a) spanwise and (b) vertical velocity fluctuations.

proximately the top of the domain, these data are presented in a linear scale. In this region the higher-order moments of the vertical velocity seem to be fitted well by

$$\langle w'^{+2p} \rangle^{1/p} = -C_p \frac{z}{H} + D_p. \quad (3.4)$$

We find that  $C_p \approx 1.08, 1.81, 2.53, 3.29, 4.17$  for  $p = 1, 2, 3, 4, 5$ , respectively. Interestingly, this means that  $C_p$  increases almost linearly as function of  $p$  (Gaussian prediction).

#### 4. Summary and conclusions

We have used large-eddy simulations (LES) to study the scaling of higher-order moments in high Reynolds number turbulent wall-bounded flow. In the LES used here, the sub-grid scale stresses are modeled using a dynamic eddy viscosity sub-grid scale model, while the stress at the wall is modeled using a log-law based closure for rough surfaces. The focus of the study is not on comparing the performance of different sub-grid closures or to explore resolution requirements in detail. Instead, the focus is on exploring the capabilities of a more or less standard LES tool in predicting the generalized logarithmic laws that have been recently observed from data at very high Reynolds numbers. We also focus on the lower-limit (distance to the wall) of the generalized logarithmic law for moments observed near the wall in LES, on exploring whether trends observed in experimental data as function of Reynolds number (viscous scales) can be discerned when the latter are replaced by possible scalings with grid scale  $\Delta/H$ , SGS mixing length scale  $C_s \Delta$ , or roughness scale  $z_0/H$ .

In terms of reproducing a logarithmic law for variances and higher-order moments of the streamwise velocity fluctuations, we find very good agreement between the LES and the experimental data, as long as a sufficiently fine resolution is used. In experiments the second and higher-order moments begin to deviate from the logarithmic law close to the wall due to viscous effects. Non-trivial dependencies on Reynolds numbers (i.e. viscous effects) were observed at significant distances from the wall (hundreds of wall units). In the LES, in which the viscous effects are not included explicitly, the higher-order moments also are found to deviate from the logarithmic law at some distance  $z_b/H$  from the wall. Detailed tests show that for the LES this effect is coupled to the grid scale or (almost equivalently) to the SGS mixing length used in the simulation and that  $z_b/H$  is (approximately) independent of  $z_0/H$ . While the simulations and comparisons

with experimental data show that there might be a small dependence of  $A_1$  on  $z_0/H$ , the observed trend is very weak compared to the uncertainties in the data and possible limitations of the simulations.

As all velocity components are available in the simulations, we also studied the spanwise and vertical velocity fluctuations. For the vertical velocity fluctuations we do not find any logarithmic regions. Instead, outside the logarithmic region of the streamwise velocity, the variance of vertical velocity fluctuations as well as appropriate roots of higher-order moments decrease approximately linearly with the distance from the wall. For the spanwise velocity fluctuations, the variance and the appropriate roots of higher-order moments do not show a very clear logarithmic region in the current dataset. However, we cannot exclude that significantly better resolved LES could reveal such a logarithmic region as the data for the spanwise velocity component are found to be more sensitive to numerical grid resolution than for the streamwise velocity component. The present analysis illustrates how the recently established logarithmic behavior of high-order moments in wall-bounded turbulence may be used to examine and test the accuracy of LES models with more rigor than only testing based on mean velocity profiles. It will be interesting to see how different sub-grid models, e.g. the standard Smagorinsky model, other eddy-viscosity models such as the Vreman *et al.* (1997) or the WALE model (Nicoud & Ducros 1999), or the modulated gradient model (Lu & Porté-Agel 2010, 2013), may perform in reproducing higher-order moments. We note that some models such as the modulated gradient model or the  $k$ -equation model can provide additional information about SGS variance. In addition, these tests can be used to assess how different types of wall model boundary conditions affect the results, see for example the trends shown in Stoll & Porté-Agel (2006) and the new insights about importance and coupling of stress fluctuations with outer-scale motions (Marusic *et al.* 2010).

*Acknowledgment:* C.M. is grateful to I. Marusic for collaborations on wall-bounded turbulence and for making the Melbourne wind tunnel data available for comparisons. R.J.A.M.S. was supported by the ‘Fellowships for Young Energy Scientists’ (YES!) of FOM, M.W. by DFG funding WI 3544/2-1, and C.M. by US National Science Foundation grants numbers CBET 1133800 and OISE 1243482. Most computations were performed with SURFsara resources, i.e. the Cartesius and Lisa clusters. This work was also supported by the use of the Extreme Science and Engineering Discovery Environment (XSEDE), which is supported by National Science Foundation grant number OCI-1053575.

## REFERENCES

- ALBERTSON, J. D. & PARLANGE, M. B. 1999 Surface length-scales and shear stress: implications for land-atmosphere interaction over complex terrain. *Water Resour. Res.* **35**, 2121–2132.
- ALFREDSSON, P. H., SEGALINI, A. & R. ÖRLÜ, R. 2011 A new scaling for the streamwise turbulence intensity in wall-bounded turbulent flows and what it tells us about the “outer” peak. *Phys. Fluids* **23**, 041702.
- BOU-ZEID, E., MENEVEAU, C. & PARLANGE, M. B. 2005 A scale-dependent Lagrangian dynamic model for large eddy simulation of complex turbulent flows. *Phys. Fluids* **17**, 025105.
- BRASSEUR, J. G. & WEI, T. 2010 Designing large-eddy simulation of the turbulent boundary layer to capture law-of-the-wall scaling. *Phys. Fluids* **22**, 021303.
- CALAF, M., MENEVEAU, C. & MEYERS, J. 2010 Large eddy simulations of fully developed wind-turbine array boundary layers. *Phys. Fluids* **22**, 015110.
- CHAMECKI, M. & MENEVEAU, C. 2011 Particle boundary layer above and downstream of an area source: scaling, simulations, and pollen transport. *J. Fluid Mech.* **683**, 1–26.
- CHESTER, S., MENEVEAU, C. & PARLANGE, M.B. 2007 Modeling turbulent flow over fractal trees with renormalized numerical simulation. *J. Comput. Phys.* **225**, 427–448.

- EYINK, G.L. 2008 Turbulent flow in pipes and channels as cross-stream 'inverse cascades' of vorticity. *Phys. Fluids* **20**, 125101.
- HULTMARK, M., VALLIKIVI, M., BAILEY, S.C.C. & SMITS, A.J. 2012 Turbulent pipe flow at extreme Reynolds numbers. *Phys. Rev. Lett.* **108** (9), 94501.
- HUTCHINS, N., CHAUHAN, K., MARUSIC, I., MONTY, J. P. & KLEWICKI, J. 2012 Towards reconciling the large-scale structure of turbulent boundary layers in the atmosphere and laboratory. *Bound-Lay. Meteorol.* **145** (2), 273–306.
- HUTCHINS, N., NICKELS, T. B., MARUSIC, I. & CHONG, M. S. 2009 Hot-wire spatial resolution issues in wall-bounded turbulence. *J. Fluid Mech.* **635**, 103–136.
- KANG, H. S., CHESTER, S. & MENEVEAU, C. 2003 Decaying turbulence in an active grid generated flow and comparisons with large eddy simulation. *J. Fluid Mech.* **480**, 129–160.
- VON KÁRMÁN, T. 1930 Mechanische Ähnlichkeit und Turbulenz. *Gött. Nachr.* pp. 58–76.
- KLEWICKI, J.C., FIFE, P. & WEI, T. 2009 On the logarithmic mean profile. *J. Fluid Mech.* **638**, 73–93.
- KULANDAIVELU, V. 2012 Evolution of zero pressure gradient turbulent boundary layers from different initial conditions. *PhD thesis, University of Melbourne.*
- LENSCHOW, D. H., LOTHON, M., MAYOR, S. D., SULLIVAN, P. P. & CANUT, G. 2012 A comparison of higher-order vertical velocity moments in the convective boundary layer from lidar with in situ measurements and large-eddy simulation. *Bound-Lay. Meteorol.* **143**, 107–123.
- LU, H. & PORTÉ-AGEL, F. 2010 A modulated gradient model for large-eddy simulation: Application to a neutral atmospheric boundary layer. *Phys. Fluids* **22**, 015109.
- LU, H. & PORTÉ-AGEL, F. 2013 A modulated gradient model for scalar transport in large-eddy simulation of the atmospheric boundary layer. *Phys. Fluids* **25**, 015110.
- MARUSIC, I. & KUNKEL, G.J. 2003 Streamwise turbulence intensity formulation for flat-plate boundary layers. *Phys. Fluids* **15**, 2461–2464.
- MARUSIC, I., MATHIS, R. & HUTCHINS, N. 2010 Predictive model for wall-bounded turbulent flow. *Science* **329**, 193–196.
- MARUSIC, I., MONTY, J.P., HULTMARK, M. & SMITS, A.J. 2013 On the logarithmic region in wall turbulence. *J. Fluid Mech.* **716**, R3.
- MENEVEAU, C. & MARUSIC, I. 2013 Generalized logarithmic law for high-order moments in turbulent boundary layers. *J. Fluid Mech.* **719**, R1.
- METZGER, M. M. & KLEWICKI, J. C. 2001 A comparative study of near-wall turbulence in high and low reynolds number boundary layers. *Phys. Fluids* **13**, 692.
- MILLIKAN, C. M. 1938 A critical discussion of turbulent flows in channels and circular tubes. *In Proceedings of the Fifth International Congress for Applied Mechanics, Harvard and MIT, 12-26 September. Wiley.*
- MOENG, C.-H. 1984 A large-eddy simulation model for the study of planetary boundary-layer turbulence. *J. Atmos. Sci.* **41**, 2052–2062.
- MOENG, C. H. & ROTUNNO, R. 1990 Vertical velocity skewness in the buoyancy-driven boundary layer. *Bound-Lay. Meteorol.* **47**, 1149–1162.
- NICOUD, F. & DUCROS, F. 1999 Subgrid-scale stress modelling based on the square of the velocity gradient tensor. *Flow, Turbulence and Combustion* **62**, 183–200.
- PERRY, A. E. & CHONG, M. 1982 On the mechanism of wall turbulence. *J. Fluid Mech.* **119**, 173–217.
- PERRY, A. E., HENBEST, S. M. & CHONG, M. 1986 A theoretical and experimental study of wall turbulence. *J. Fluid Mech.* **165**, 163–199.
- PERRY, A. E., LIM, K. L. & HENBEST, S. M. 1987 An experimental study of the turbulence structure in smooth- and rough-wall boundary layers. *J. Fluid Mech.* **177**, 437.
- PORTÉ-AGEL, F., MENEVEAU, C. & PARLANGE, M. B. 2000 A scale-dependent dynamic model for large-eddy simulation: application to a neutral atmospheric boundary layer. *J. Fluid Mech.* **415**, 261–284.
- PRANDTL, L. 1925 Bericht über Untersuchungen zur ausgebildeten Turbulenz. *Z. Angew. Math. Mech.* **5**, 136–139.
- SCHULTZ, M. P. & FLACK, K. A. 2007 The rough-wall turbulent boundary layer from the hydraulically smooth to the fully rough regime. *J. Fluid Mech.* **580**, 381–405.

- SCOTTI, A., MENEVEAU, C. & LILLY, D. K. 1993 Generalized Smagorinsky model for anisotropic grids. *Physics of Fluids A- Fluid Dynamics* **5**, 2306–2308.
- SMITS, A. J., MCKEON, B. J. & MARUSIC, I. 2011 High Reynolds number wall turbulence. *Annu. Rev. Fluid Mech.* **43**, 353–375.
- STOLL, R. & PORTÉ-AGEL, F. 2006 Effects of roughness on surface boundary conditions for large-eddy simulation. *Bound-Lay. Meteorol.* **118**, 169–187.
- SULLIVAN, P. P. & PATTON, E. G. 2011 The effect of mesh resolution on convective boundary layer statistics and structures generated by large-eddy simulation. *J. of the Atmospheric Sciences* **68**, 2395–2415.
- TOWNSEND, A. A. 1976 Structure of turbulent shear flow, 2nd edn. *Cambridge University Press*.
- VREMAN, B., GEURTS, B. & KUERTEN, H. 1997 Large-eddy simulation of the turbulent mixing layer. *J. Fluid Mech.* **339**, 357–390.
- WEI, T., FIFE, P., KLEWICKI, J. C. & MCMURTRY, P. 2005 Properties of the mean momentum balance in turbulent boundary layer, pipe and channel flows. *J. Fluid Mech.* **522**, 303–327.
- WINKEL, E. S., CUTBIRTH, J. M., CECCIO, S. L., PERLIN, M. & DOWLING, D. R. 2012 Turbulence profiles from a smooth flat-plate turbulent boundary layer at high Reynolds number. *Exp. Therm. Fluid Sci.* **40**, 140–149.
- ZAGAROLA, M.V. & SMITS, A. J. 1998 Mean-flow scaling of turbulent pipe flow. *J. Fluid Mech.* **373**, 33–79.